Title

Atomic scale interface engineering for realizing a perpendicularly magnetized CoFeB-based skyrmion hosting material

Journal

Applied Physics Letters, 122(24)

ISSN

0003-6951

Authors

Lee, Sang Sun

Ju, Tae-Seong

Han, Hee-Sung

et al.

Publication Date

2023-06-12

DOI

10.1063/5.0153777

Peer reviewed

Atomic scale interface engineering for realizing a perpendicularly magnetized CoFeB-based skyrmion hosting material

Sang Sun Lee[1], Tae-Seong Ju[1], Changsoo Kim[1], Kyoung-Woong Moon[1,], and Seungmo Yang[1,*]*

[1]*Quantum Spin Team, Korea Research Institute of Standards and Science, Daejeon, 34113, Republic of Korea*

[*]Corresponding author

E-mail address: kwmoon@kriss.re.kr (Kyoung-Woong Moon), justin.yang@kriss.re.kr (Seungmo Yang)

Abstract

Néel-type magnetic skyrmions in perpendicularly magnetized systems have attracted considerable interest due to their potential in fundamental research on topological objects and spintronics applications. Various systems have been explored to study Néel-type magnetic skyrmions, including repeated magnetic multilayers, 2-dimensional materials, and single magnetic thin-films. Among these, single magnetic thin-films, especially a CoFeB single layer, offers multiple benefits such as reduced defect energy, high mobility, and easy integration with existing magnetoresistive random access memory technology. However, optimizing CoFeB-based skyrmion hosting materials remains challenging and requires further systematic and comprehensive investigation. In this study, we examine the effect of atomic-scale interface engineering by inserting a Ta layer between the CoFeB/MgO interface on perpendicular magnetic anisotropy, saturation magnetization, and Dzyaloshinskii-Moriya interaction.

Moreover, we provide a guideline for engineering material parameters and demonstrate the validity of atomic-scale interface engineering. Our findings contribute to the development of optimized CoFeB-based skyrmion hosting materials.

The topologically non-trivial spin configuration of magnetic skyrmions exhibit exotic phenomena, making them a promising platform for fundamental research on topological objects as well as spintronics applications[1]. In particular, the study of Neel-type magnetic skyrmions in a perpendicularly magnetized system has been the focus of intense research, aimed at demonstrating topology-related physics phenomena such as the skyrmion Hall effect[2], the topological Hall effect[3], and additional topological barrier[4]. Due to the non-collinear spin configuration of magnetic skyrmions, the Heisenberg exchange interaction, which favors parallel alignment of neighbor spins in a ferromagnet, is unable to stabilize them. The energy of magnetic skyrmions in perpendicularly magnetized systems is determined by the competition between the perpendicular magnetic anisotropy (PMA), magnetic dipole-dipole interactions, and the Dzyaloshinskii-Moriya interaction (DMI)[5]. The PMA energy plays a crucial role in forming magnetic skyrmions in perpendicularly magnetized systems by providing a two-fold potential energy configuration. Additionally, it is important to note that magnetic skyrmions consist of three distinct components: a core, a background, and a domain wall (DW), as depicted in Figure 1a. The PMA increases the energy of magnetizations in a film plane, thus contributing to an overall increase in the energy of skyrmions by increasing the energy of DWs. On the other hand, the magnetic dipole-dipole interaction favors a magnetic skyrmion state as the dipolar magnetic fields generated by the background magnetizations lower the energy of the core of a magnetic skyrmion, as depicted in Figure 1b. Additionally, the Dzyaloshinskii-Moriya interaction (DMI) also favors a magnetic skyrmion due to its preference for non-collinear spin textures. The DMI also determines the chirality of a magnetic skyrmion, as described in Figure 1b. Therefore, to achieve a stable magnetic skyrmion in a perpendicularly magnetized system, it is necessary to decrease the effective PMA energy density per volume (K_{ef}), increase the DMI energy density per area (D), or increase the energy of the magnetic dipole-dipole interaction ($\mu_0 M_s^2 d^2$), where μ_0 is the magnetic permeability,

M_S is the saturation magnetization, and d is the thickness of the ferromagnetic layer. To obtain a skyrmion hosting material, some research has utilized multilayered systems of [heavy metal/ferromagnet/heavy metal or oxide layer]$_n$ with more than ten repetition numbers (n) to maximize the dipole-dipole interaction energy by increasing the total ferromagnetic layer thickness[6,7]. On the other hand, other groups have employed a heavy metal/CoFeB/MgO structure, where an atomically thin metal layer is typically inserted between the CoFeB/MgO layer[8]. As the PMA in CoFeB/MgO systems originates from the hybridization of Fe 3d/O 2p orbitals at the interface[9], the atomically thin inserted metal layer can manipulate the PMA with extreme precision. A CoFeB/MgO structure is an essential component of a magnetic tunnel junction (MTJ)[10], making it easy to integrate with existing magnetoresistive random-access memory (MRAM) technology. Additionally, compared to multilayered systems, a magnetic skyrmion in a single and thin (~ 1 nm) ferromagnet system such as a CoFeB/MgO system is relatively easy to move by electrical current because the total energy to overcome pinning energy barriers is smaller due to its smaller volume[11]. Based on these advantages, various research on magnetic skyrmions has been reported in CoFeB-MgO-based structures. However, obtaining CoFeB-based skyrmion hosting materials by optimizing the inserted metal layer has yet to be systematically investigated. In this work, we investigate the effect of atomic-scale interface engineering using an ultra-thin inserted Ta layer on PMA, DMI, saturation magnetization, and provide a guideline for engineering material parameters. Furthermore, we demonstrate the validity of atomic scale thickness control.

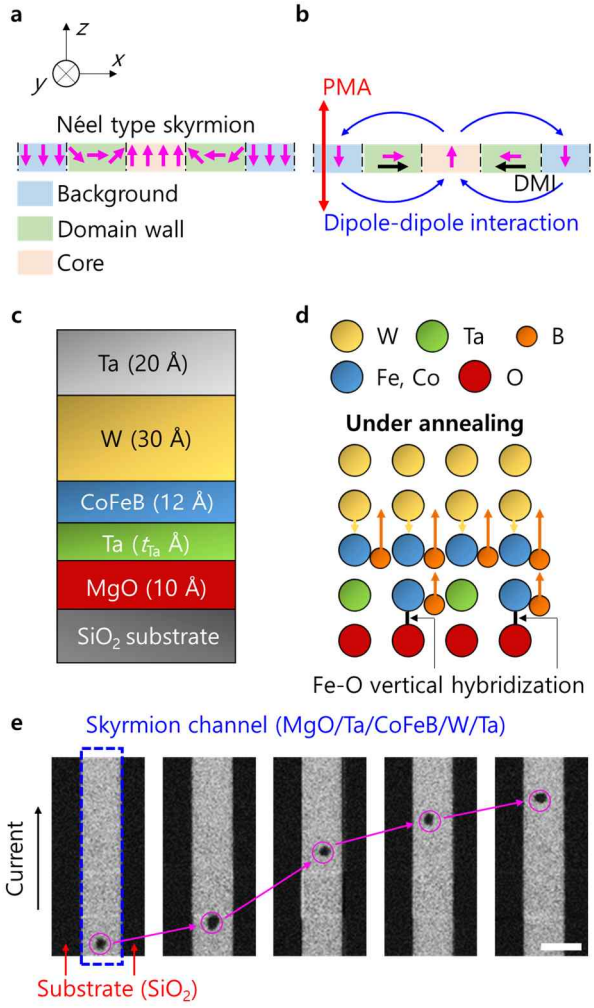

Figure 1. Schematics for magnetic Néel type skyrmion configuration and sample structure. a. A cross section of Magnetic Néel type skyrmion configuration consist of three parts: background, domain wall, and core. **b.** Competing interactions presenting in a magnetic Néel type skyrmion. **c.** Investigated sample structures of SiO_2(Substrate)/MgO/Ta/CoFeB/W/Ta. **d.** Schematics of ion diffusion behavior during annealing process. **e.** Current-induced magnetic Néel type skyrmion dynamics, ensuring the Néel type domain wall configuration. Scale bar, 10 μm.

Figure 1c illustrates the investigated structures of Si substrate/SiO_2 (3000 Å)/MgO (10 Å)/Ta (t_{Ta} Å)/CoFeB (12 Å)/W (30 Å)/Ta (20 Å) samples, where t_{Ta} is the thickness of an inserted Ta

layer. These samples were fabricated using magnetron sputtering with a base pressure of $\sim 7 \times 10^{-9}$ Torr, followed by a post-annealing process at various temperatures under $\sim 5 \times 10^{-8}$ Torr. The post-annealing process at moderate temperature promotes the diffusion of boron ions from the CoFeB layer into a W layer because the enthalpy of W-B bonding is less than that of Co or Fe-B bonding[12]. The diffusion of boron ions out of the CoFeB layer results in the rearrangement of the CoFeB-MgO interface and an increase in the formation of Fe-O vertical bondings, leading to an enhancement in the PMA[13].

However, at higher temperatures, the post-annealing process can lead to the diffusion of W or Ta atoms into the CoFeB layer. This intermixing of W or Ta atoms with the CoFeB layer results in deterioration of both the PMA and M_S by forming a magnetically dead layer, as shown in Figure 1d[14]. In this system, a magnetic skyrmion can be stabilized when the ratio of material parameters, PMA, M_S, and DMI, is within a specific range. As an example, a Si substrate/SiO_2 (3000 Å)/MgO (10 Å)/Ta (1.10 Å)/CoFeB (12 Å)/W (30 Å)/Ta (20 Å) structure with a 270 °C post-annealing process can host magnetic skyrmions as demonstrated in Figure 1e, where the chirality is also confirmed by the skyrmion movement via spin-orbit torque (SOT) as shown in Figure 1e[6].

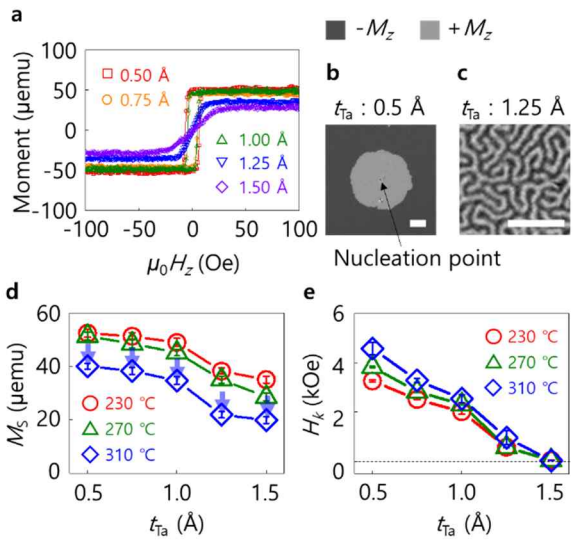

Figure 2. Saturation magnetization and perpendicular magnetic anisotropy features. a. Out-of-plane magnetic hysteresis loops as a function of the inserted Ta layer thickness followed by 270 ℃ annealing process. **b-c.** MOKE images of magnetic domains of **b,** a thin (0.5 Å) inserted Ta layer sample and **c,** a relatively thick (1.25 Å) inserted Ta layer sample. Scale bar, 10 μm. **d.** Saturation magnetization and **e.** effective perpendicular magnetic anisotropy field as a function of the inserted Ta thickness layer with various annealing temperature.

Figure 2a displays the out-of-plane magnetic hysteresis loops of a Si substrate/SiO_2 (3000 Å)/MgO (10 Å)/Ta (t_{Ta} Å)/CoFeB (12 Å)/W (30 Å)/Ta (20 Å) structure after a 270 °C post-annealing process, where the thickness of the inserted Ta layer ranges from 0.50 Å to 1.50 Å with an increment of 0.25 Å. As the thickness of the inserted Ta layer is decreased (t_{Ta} = 0.50 ~ 0.10 Å), the out-of-plane hysteresis loops in Figure 2a exhibit a characteristic square shape, indicating a pronounced PMA property. As the thickness of the inserted Ta layer increases (t_{Ta} = 1.25 ~ 1.50 Å), the out-of-plane hysteresis loops undergo a transition to a tilted graph shape, with a corresponding decrease in the remanence magnetization ($M_{\mathrm{r}} \equiv M(H = 0)/M_{\mathrm{s}}$) approaching zero. To further investigate the detailed domain states, we employed a Magneto-Optic Kerr Effect (MOKE) microscopy system, as illustrated in Figure 2b and c. The sample with t_{Ta} = 0.50 Å, which exhibits a square-shaped hysteresis loop, displays nucleation and circular expansion of domains. It is commonly observed in films with typical PMA. However, the sample with t_{Ta} = 1.25 Å and a tilted hysteresis loop shows a stripe domain state as depicted in Figure 2c. Therefore, the observed zero M_{r} values are a result of the net zero magnetic moment of a spontaneously generated stripe domain state at zero magnetic field, rather than a magnetic anisotropy easy axis transition to an in-plane direction. The stripe domain state serves as a crucial starting point for the generation of magnetic skyrmions, as the energy of a stripe domain state is comparable to that of a magnetic skyrmion state[11].

Furthermore, Figure 2d and e illustrate the M_s and the effective PMA field (H_k) as a function of the inserted Ta thickness layer in a Si substrate/SiO_2 (3000 Å)/MgO (10 Å)/Ta (t_{Ta} Å)/CoFeB (12 Å)/W (30 Å)/Ta (20 Å) sample with various post-annealing temperatures. Here, the H_k value is defined by the relation of $K_{ef} \equiv \mu_0 M_s H_k/2$. It was observed that both the M_s and H_k values decrease with an increase in the inserted Ta layer thickness. This trend can be attributed to the fact that the inserted Ta layer deteriorates the PMA, as shown in Figure 1d, and also leads to a thicker magnetically dead layer.

Furthermore, the annealing temperature dependence of the H_k and M_s was also investigated. As shown in Figure 2d, the M_s value is observed to decrease with an increase in post-annealing temperatures, which suggests that a higher post-annealing temperature results in a thicker intermixed magnetically dead layer. This trend is likely caused by the fact that Ta atoms are more mobile than W atoms due to their lower cohesive energy.

Previous studies have established that diffusion of Ta atoms into a CoFeB layer begins at a post-annealing temperature of 250 °C[14], while diffusion of W atoms commences at 300 °C[15]. As a result, the significant decline in saturation magnetization observed at 310 °C in Figure 2d (blue arrows) can be attributed to the additional diffusion of W atoms. Figure 2e depicts the H_k values at various post-annealing temperatures. The H_k values increase as the post-annealing temperature is elevated, in contrast to the trend observed in the case of saturation magnetization. During post-annealing at temperatures of 230, 270, and 310 °C, diffusion of B atoms out of the CoFeB layer increases the H_k values. As the Ta atoms already existing between the CoFeB-MgO layers inhibit vertical Fe-O bondings, they do not contribute to the variations in H_k values observed with changes in post-annealing temperatures. In addition, W atoms do not impact the H_k values in the current study as they only begin diffusing towards the CoFeB/MgO interface at 310°C.

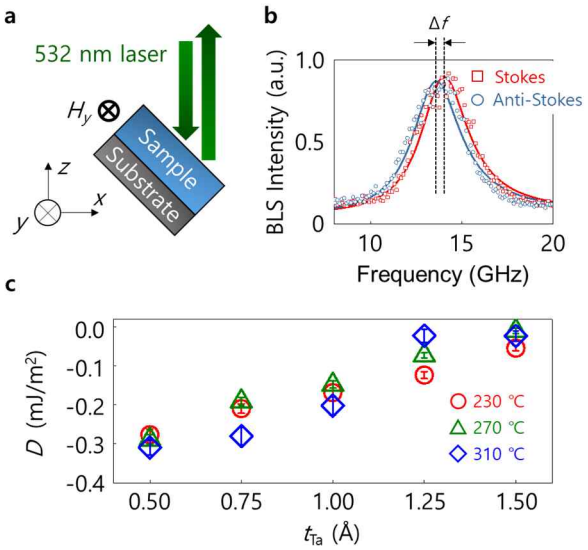

Figure 3. Dzyaloshinskii-Moriya interaction energy density. a. Schematics of Brillouin Light Scattering analysis for estimating Dzyaloshinskii-Moriya interaction energy density. **b.** BLS spectra of Stokes and anti-Stokes. **c.** Dzyaloshinskii-Moriya interaction energy density as a function of the inserted Ta thickness layer with various annealing temperature.

Another critical parameter for determining skyrmion stability is DMI, which serves to reduce domain wall energy and stabilize the swirling spin texture, including a skyrmion. In our structure, DMI is known to originate from both the W/CoFeB and CoFeB/MgO interfaces. Therefore, the complicated intermixing ions after post-annealing process can modify the DMI values. To conform the DMI values, we utilized a Brillouin Light Scattering (BLS) system as shown in Figure 3a. The Damon-Eshbach mode of spin waves propagates at the upper and lower interfaces of a ferromagnetic thin-film. It is well known[16] that the presence of interfacial DMI by symmetry breaking at the interface of a magnetic thin-film induces nonreciprocity of the Damon-Eshbach spin wave mode as below:

$$f_{\mathrm{DE}} = f_0 + \frac{\gamma D}{\pi M_{\mathrm{S}}} k$$

Here, D represents the interfacial DMI energy density in J/m^2 units. Therefore, the frequency difference between Stokes (+k) and anti-Stokes (-k) is

$$\Delta f = \frac{2\gamma D}{\pi M_S} k$$

Employing the aforementioned equation, the DMI energy density can be derived from the measured Δf as shown in Figure 3b. With the measured M_S and k (0.87×10^6 A/m and $0.0167\ \mathrm{nm}^{-1}$), D values are determined as a function of the inserted Ta thicknesses and the post-annealing temperatures, as presented in Figure 3c. DMI values approaches to zero with increasing the inserted Ta thickness regardless of the post-annealing temperature. It indicates that the reduction of DMI is attributed to the CoFeB/MgO interface modulation by inserting Ta layer, rather than a change in the W/CoFeB interface because W atoms do not diffuse under lower annealing temperature such as 230 ℃.

We systematically investigated three critical parameters, PMA, M_S and DMI, as a function of the inserted Ta thickness following a post-annealing process under various temperatures. The skyrmion stability is determined as a function of stripe domain width under zero-field, which can be expressed[17]:

$$\lambda \propto e^{\left(\frac{\pi\sigma_w}{\mu_0 M_S^2 d}\right)}$$

, where σ_w represents the domain wall energy density. In the presence of DMI, the Néel-type domain wall energy density can be described as follows:

$$\sigma_w \cong 4\sqrt{AK_{ef}} - \pi D$$

Consequently, skyrmion stability can be determined by $\frac{4\sqrt{AK_{ef}}-\pi D}{\mu_0 M_S^2 d}$, where all parameters have been measured in the previous experiments. Figure 4a illustrates a plot of $\frac{4\sqrt{AK_{ef}}-\pi D}{\mu_0 M_S^2 d}$ as a function of the inserted Ta thickness with various annealing temperatures. Note that the

results of continuously varying thickness samples after 230 ℃ annealing process have been added to Figure 4a, providing a detailed change in domain structures. Figure 4b-f present MOKE images of five samples with various $\frac{4\sqrt{AK_{\mathrm{eff}}}-\pi D}{\mu_0 M_S^2 d}$ values, under zero and a particular H_z field. Figure 4b shows a clear circular domain expansion under zero H_z field after domain nucleation because the sample has a high $\frac{4\sqrt{AK_{\mathrm{eff}}}-\pi D}{\mu_0 M_S^2 d}$ value, indicating a large stripe domain width. It is worth noting that the stripe domain width is exponentially proportional to a $\frac{4\sqrt{AK_{\mathrm{eff}}}-\pi D}{\mu_0 M_S^2 d}$ value. Figure 4c presents higher domain wall roughness than that in Figure 4b due to the reduced domain wall energy, which favors small stripe domain width. Figure 4d presents a spontaneously stripe domain structure because a $\frac{4\sqrt{AK_{\mathrm{eff}}}-\pi D}{\mu_0 M_S^2 d}$ value of about 9.5 induces the stripe domain with small width to be more stable. However, applying a H_z field cannot yet generate any skyrmion due to high energy barrier to transform stripe domains into a skyrmion state as shown in the bottom image of Figure 4d. Samples with smaller values of $\frac{4\sqrt{AK_{\mathrm{eff}}}-\pi D}{\mu_0 M_S^2 d}$ than 9 also show a spontaneously generated stripe domain structure under zero H_z field. In addition, applying particular H_z fields generate a bunch of skyrmions as shown in Figure 4e and f. This is because the energy barrier to transform stripe domains into a skyrmion state is proportional to the stripe domain width, which is exponentially proportional to $\frac{4\sqrt{AK_{\mathrm{eff}}}-\pi D}{\mu_0 M_S^2 d}$[11]. Therefore, we can conclude that a value of $\frac{4\sqrt{AK_{\mathrm{eff}}}-\pi D}{\mu_0 M_S^2 d}$ in a perpendicularly magnetized thin-film can be a guideline for optimizing CoFeB-based skyrmion host materials. A $\frac{4\sqrt{AK_{\mathrm{eff}}}-\pi D}{\mu_0 M_S^2 d}$ value from 8 to 10 can spontaneously generate stripe domains under zero H_z field, but cannot generate skyrmions only by applying a H_z field, while a $\frac{4\sqrt{AK_{\mathrm{eff}}}-\pi D}{\mu_0 M_S^2 d}$ value below 9 can also create skyrmions by cutting stripe domains under a particular H_z field.

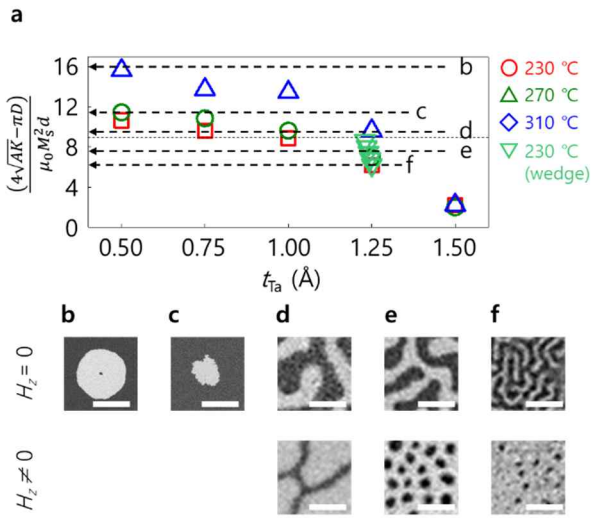

Figure 4. A new parameter for optimizing CoFeB-based skyrmion hosting materials. a. Plot of a newly adopted parameter of all investigated samples, and additional wedged samples. b, Magnetic Néel type skyrmion configuration consist of three parts: background, domain wall, and core. **b-f.** MOKE images under zero-field (top) and a specific perpendicular magnetic field (bottom), as a function of varying $\frac{4\sqrt{AK_{\mathbf{eff}}}-\pi D}{\mu_0 M_S^2 d}$ values. **b-c.** Scale bar, 40 μm. **d-f.** Scale bar, 10 μm.

Finally, we discuss the validity of the ultra-thin thickness variation in the inserted layer. When considering the inserted Ta layer thickness ranging from 1.25 to 1.50 Å, island growth becomes evident as the thickness is either less than or comparable to the interatomic radius of Ta atoms, corresponding to an ideal Ta monolayer thickness of approximately 1.25 Å. In magnetic thin-film systems, the magnetic exchange length (l_{ex}) plays a crucial role, as it represents the distance over which spins are uniformly aligned, behaving as a single spin due to the Heisenberg exchange interaction, as depicted in Figure 5a. As a result, local effects of island atoms on individual spins are evenly distributed among all magnetic moments within

the exchange area, which is equivalent to the square of the magnetic exchange length (l_{ex}^2) as in Figure 5b. To determine the magnetic exchange length, we apply the well-known equation[18]:

$$l_{\mathrm{ex}} = \sqrt{\frac{A}{(\mu_0 M_S^2/2)}}$$

, where A is the exchange stiffness. Using the previously reported exchange stiffness value for a one nm-thick CoFeB layer (12 pJ/m) [19] and the measured magnetization (0.87×10^6 A/m), we calculated the magnetic exchange length (l_{ex}) as 9.40 nm. Furthermore, we can define the effective thickness of the inserted layer as the average inserted thickness on the exchange area. For example, when a perfect Ta monolayer covers the entire exchange area, the effective thickness of the Ta layer is equal to the interatomic radius (r_{Ta}), or the monolayer thickness. In contrast, if just one Ta atom exists within the exchange area, the effective thickness of the Ta layer is the interatomic radius divided by the total number of magnetic atoms in the exchange area, as described in Figure 4c. This model can be clarified from the experimental results. Using the PMA energy density equation of $K_{\mathrm{ef}} = \frac{1}{2}\mu_0 M_{\mathrm{s}} H_{\mathrm{k}} = K_{\mathrm{u}} - \frac{1}{2}\mu_0 M_{\mathrm{S}}^2$, when K_{u} is zero, H_{k} equals to $-M_{\mathrm{s}}$. Figure 5d shows a plot of the H_k values as a function of the Ta interlayer effective thickness. The linear fit reveals that the Ta thickness corresponding to $H_{\mathrm{k}} = -M_{\mathrm{s}}$ is 1.55 Å, which is almost identical to the reported Ta interatomic radius. Additionally, based on the calculated exchange length, we estimate that approximately there are approximately 1,000 Fe (or Co) atoms in the exchange area. Then, one Ta atom corresponds to the effective thickness of 0.00125 Å, which is considerably smaller than the thickness variation step in our experiment, thus validating our experimental approach.

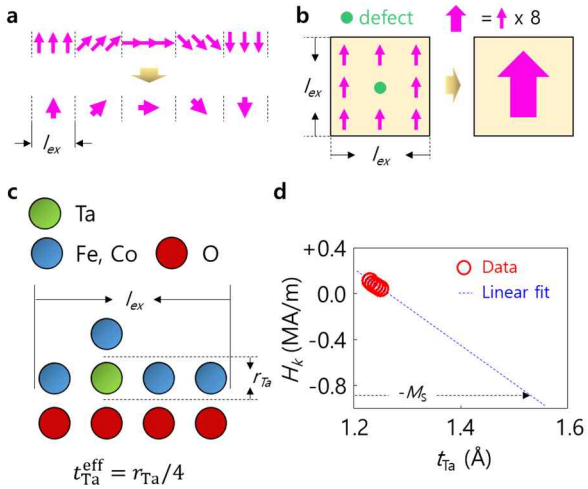

Figure 5. Validity of the atomic-scale interface engineering experiment. a. Concept of the magnetic exchange length. **b.** Schematics of the role of defects, taking into account the magnetic exchange length in a thin-film system. **c.** Schematics of the effective thickness concept. **d.** Estimation of the effective thickness of an ideally covered monolayer Ta layer.

In conclusion, we systemically investigated material parameters of PMA, M_S, and DMI with atomic-scale interface engineering of a Ta layer between the CoFeB/MgO interface under various post-annealing temperature. Then, we introduced a new parameter of $\frac{4\sqrt{AK_{eff}}-\pi D}{\mu_0 M_S^2 d}$, which can be used as a guideline for optimizing materials parameters to obtain a CoFeB-based skyrmion hosting material. Under a $\frac{4\sqrt{AK_{eff}}-\pi D}{\mu_0 M_S^2 d}$ value below 9, magnetic skyrmions can be spontaneously generated just by applying a perpendicular magnetic field. Finally, we have demonstrated the validity of the atomic-scale interface engineering in a magnetic thin-film by introducing the concept of a magnetic exchange length and the effective thickness. We believe that our work paves the way for fabrication of improved CoFeB-based skyrmion hosting materials, promoting skyrmion-based research.

Acknowledgements

This work was supported by the National Research Foundation of Korea (Grant No. NRF-2021M3F3A2A01037663 and NRF-2022M3H4A1A04071154).

References

1 Naoto Nagaosa and Yoshinori Tokura, Nature Nanotechnology **8** (12), 899 (2013); C. Back, V. Cros, H. Ebert, K. Everschor-Sitte, A. Fert, M. Garst, Tianping Ma, S. Mankovsky, T. L. Monchesky, M. Mostovoy, N. Nagaosa, S. S. P. Parkin, C. Pfleiderer, N. Reyren, A. Rosch, Y. Taguchi, Y. Tokura, K. von Bergmann, and Jiadong Zang, Journal of Physics D: Applied Physics **53** (36), 363001 (2020).

2 Wanjun Jiang, Xichao Zhang, Guoqiang Yu, Wei Zhang, Xiao Wang, M. Benjamin Jungfleisch, John E Pearson, Xuemei Cheng, Olle Heinonen, Kang L. Wang, Yan Zhou, Axel Hoffmann, and Suzanne G E te Velthuis, Nature Physics **13** (2), 162 (2017); Kai Litzius, Ivan Lemesh, Benjamin Krüger, Pedram Bassirian, Lucas Caretta, Kornel Richter, Felix Büttner, Koji Sato, Oleg A. Tretiakov, Johannes Förster, Robert M. Reeve, Markus Weigand, Iuliia Bykova, Hermann Stoll, Gisela Schütz, Geoffrey S. D. Beach, and Mathias Kläui, Nature Physics **13** (2), 170 (2017).

3 Takashi Kurumaji, Taro Nakajima, Max Hirschberger, Akiko Kikkawa, Yuichi Yamasaki, Hajime Sagayama, Hironori Nakao, Yasujiro Taguchi, Taka-hisa Arima, and Yoshinori Tokura, Science **365** (6456), 914 (2019); Qiming Shao, Yawen Liu, Guoqiang Yu, Se Kwon Kim, Xiaoyu Che, Chi Tang, Qing Lin He, Yaroslav Tserkovnyak, Jing Shi, and Kang L. Wang, Nature Electronics **2** (5), 182 (2019); M. Raju, A. P. Petrović, A. Yagil, K. S. Denisov, N. K. Duong, B. Göbel, E. Şaşıoğlu, O. M. Auslaender, I. Mertig, I. V. Rozhansky, and C. Panagopoulos, Nature Communications **12** (1), 2758 (2021).

4 Soong-Geun Je, Hee-Sung Han, Se Kwon Kim, Sergio A. Montoya, Weilun Chao, Ik-Sun Hong, Eric E. Fullerton, Ki-Suk Lee, Kyung-Jin Lee, Mi-Young Im, and Jung-Il Hong, ACS Nano **14** (3), 3251 (2020); A. W. D. Leishman, R. M. Menezes, G. Longbons, E. D. Bauer, M. Janoschek, D. Honecker, L. DeBeer-Schmitt, J. S. White, A. Sokolova, M. V. Milošević, and M. R. Eskildsen, Physical Review B **102** (10), 104416 (2020).

5 Seungmo Yang, Tae-Seong Ju, Changsoo Kim, Hyun-Joong Kim, Kyongmo An, Kyoung-Woong Moon, Sungkyun Park, and Chanyong Hwang, Nano Letters **22** (21), 8430 (2022); Felix Büttner, Ivan Lemesh, and Geoffrey S. D. Beach, Scientific Reports **8** (1), 4464 (2018).

6 Seonghoon Woo, Kai Litzius, Benjamin Krüger, Mi-Young Im, Lucas Caretta, Kornel Richter, Maxwell Mann, Andrea Krone, Robert M. Reeve, Markus Weigand, Parnika Agrawal, Ivan Lemesh, Mohamad-Assaad Mawass, Peter Fischer, Mathias Kläui, and Geoffrey S. D. Beach, Nature Materials **15** (5), 501 (2016).

7 Anjan Soumyanarayanan, M. Raju, A. L. Gonzalez Oyarce, Anthony K. C. Tan, Mi-Young Im, A. P Petrović, Pin Ho, K. H. Khoo, M. Tran, C. K. Gan, F. Ernult, and C. Panagopoulos, Nature Materials **16** (9), 898 (2017).

8 Felix Büttner, Ivan Lemesh, Michael Schneider, Bastian Pfau, Christian M. Günther, Piet Hessing, Jan Geilhufe, Lucas Caretta, Dieter Engel, Benjamin Krüger, Jens Viefhaus, Stefan Eisebitt, and Geoffrey S. D. Beach, Nature Nanotechnology **12** (11), 1040 (2017); Seungmo Yang, Jong Wan Son, Tae-Seong Ju, Duc Minh Tran, Hee-Sung Han, Sungkyun Park, Bae Ho Park, Kyoung-Woong Moon, and Chanyong Hwang, Advanced Materials **35** (9), 2208881 (2023); Seungmo Yang, Kyoung-Woong Moon, Tae-Seong Ju, Changsoo Kim, Hyun-Joong Kim, Juran Kim, Bao Xuan Tran, Jung-Il Hong, and Chanyong Hwang, Advanced Materials **33** (45), 2104406

(2021); Jakub Zázvorka, Florian Jakobs, Daniel Heinze, Niklas Keil, Sascha Kromin, Samridh Jaiswal, Kai Litzius, Gerhard Jakob, Peter Virnau, Daniele Pinna, Karin Everschor-Sitte, Levente Rózsa, Andreas Donges, Ulrich Nowak, and Mathias Kläui, Nature Nanotechnology **14** (7), 658 (2019); Moojune Song, Mujin You, Seungmo Yang, Tae-Seong Ju, Kyoung-Woong Moon, Chanyong Hwang, Kyoung-Whan Kim, Albert Min Gyu Park, and Kab-Jin Kim, Advanced Materials **34** (40), 2203275 (2022).

9 S. Ikeda, K. Miura, H. Yamamoto, K. Mizunuma, H. D. Gan, M. Endo, S. Kanai, J. Hayakawa, F. Matsukura, and H. Ohno, Nature Materials **9** (9), 721 (2010); A. Hallal, H. X. Yang, B. Dieny, and M. Chshiev, Physical Review B **88** (18), 184423 (2013).

10 T. Na, S. H. Kang, and S. O. Jung, IEEE Transactions on Circuits and Systems II: Express Briefs **68** (1), 12 (2021).

11 Kyoung-Woong Moon, Seungmo Yang, Tae-Seong Ju, Changsoo Kim, Byoung Sun Chun, Sungkyun Park, and Chanyong Hwang, NPG Asia Materials **13** (1), 20 (2021).

12 A. K. Niessen and F. R. De Boer, Journal of the Less Common Metals **82**, 75 (1981).

13 Zhongchang Wang, Mitsuhiro Saito, Keith P. McKenna, Shunsuke Fukami, Hideo Sato, Shoji Ikeda, Hideo Ohno, and Yuichi Ikuhara, Nano Letters **16** (3), 1530 (2016).

14 N. Miyakawa, D. C. Worledge, and K. Kita, IEEE Magnetics Letters **4**, 1000104 (2013).

15 Gwang-Guk An, Ja-Bin Lee, Seung-Mo Yang, Jae-Hong Kim, Woo-Seong Chung, and Jin-Pyo Hong, Acta Materialia **87**, 259 (2015).

16 Jaehun Cho, Nam-Hui Kim, Sukmock Lee, June-Seo Kim, Reinoud Lavrijsen, Aurelie Solignac, Yuxiang Yin, Dong-Soo Han, Niels J. J. van Hoof, Henk J. M. Swagten, Bert Koopmans, and Chun-Yeol You, Nature Communications **6** (1), 7635 (2015).

17 T. N. G. Meier, M. Kronseder, and C. H. Back, Physical Review B **96** (14), 144408 (2017).

18 G. S. Abo, Y. K. Hong, J. Park, J. Lee, W. Lee, and B. C. Choi, IEEE Transactions on Magnetics **49** (8), 4937 (2013).

19 Gyung-Min Choi, Journal of Magnetism and Magnetic Materials **516**, 167335 (2020).